Fe-Si NANOSTRUCTURED COATING ON 48 XC STEEL DEVELOPED BY MECHANICALLY ALLOYED

Ali MAMERI[1*], Ismail DAOUD[2], Rachid BELKADA[1], Amar MANSERI[1], Merzak LARIBI[3]

In this work, our objective was to develop a nanostructured Fe_xSi_y coating on an XC steel substrate using a mechanical alloying. The results revealed that milling time and Si ratio (%) have significant influence on particle size, morphology, and phase formed. In the second phase of our investigation, the intermetallic formed were deposit on the XC48 substrate via mechanical alloying. The co-milling of substrates/alloyed powder was applied for different durations and subjected to heat treatments at various temperatures. The microstructural analysis, performed using optical microscopy and Scanning Electron Microscopy techniques, revealed a coating with a thickness of approximately 150 µm.

Keywords: Fe-Si, nanostructured, intermetallic, mechanical alloying, coating

1. Introduction

Mechanical alloying (MA) is a widely employed technique known for its ability to create unique structures and high material properties [1, 2]. This technique involves a sequence of cold welding, fracturing and rewelding processes under high-energy ball milling of blended material. During mechanical alloying, the composition can be changed from pure elements to a solid solution, chemical compounds, or amorphous materials [3-6]. MA provides advantages to synthesis materials, which are difficult to obtain with conventional techniques. It does not claim the miscibility of elements in the liquid state, which offers the possibility to synthesize various materials [7].

Since its development, MA has been employed to synthesize several advanced materials, such as intermetallics [7], nanocomposites [8], metallic glasses [9] and materials for energy applications [10]. In addition, this technique can be used to activate the aluminothermic reaction between reactant powders [11-14]. Fe-Si alloys are widely employed for their excellent magnetic properties [15]. FeSi compounds have a high melting point and good structural stability at

[1] Semiconductors Technology for Energetic Research Center (CRTSE), Algiers, Algeria.
*Corresponding author: mameri-ali@hotmail.fr
[2] Laboratory of Science and Materials Engineering (LSGM), University of Science and Technology Houari Boumediene, Algiers, Algeria.
[3] Metallurgy Department, Polytechnic school of Algiers, Algiers, Algeria

high temperature, which make them useful in thermal and corrosive environments [16]. Several routes were used to obtain Fe-Si compounds, depending on the final form (bulk, nanostructured, thin film, etc.). MA is a promising method for the production of Fe-Si alloys [17]. To enhance their properties, researchers have investigated numerous Fe-Si systems from amorphous to nanocrystalline FeSi materials that have been developed using MA [18-23].

The development of nanocrystalline coatings is considered a significant challenge. The use of conventional techniques, such as electrodeposition, chemical vapour deposition, and cold spraying, often leads to the destabilization of the nanocrystalline structure [24]. It has recently been demonstrated that it is possible to develop coatings using MA process while preserving the nanostructure of materials [25]. The use of MA process for coating in the Fe-Si system has not been extensively explored. Gupta and al.[24] have studied Fe 80 at%, Si 20 at% nanostructured coating on mild steel by MA, the element powder (Fe80 at%, Si 20 at%) were milled for 20 h. The pre-alloyed nanocrystalline $Fe_{80}Si_{20}$ was milled with coupon for different times (1-4 h) and different speed (150, 250, 350 rpm). They found that the highest value of thickness of 350µm was obtained at speed of 200 rpm.

The particularity of this study, that distinguishes it from previous research, lies in its novel approach to synthesizing Fe_xSi_y nanocrystalline coatings using the MA process and the subsequent optimization of treatment parameters for achieving adherent coatings

2. Experimental details

Iron (purity of 99%) and silicon (feedstock) powders were used as raw materials. To prepare Fe_xSi_y nanocrystalline powders with two stoichiometries namely $Fe_{90}Si_{10}$ and $Fe_{65}Si_{35}$, the powders were milled in a planetary ball mill (PM 200, Retsch) using the following parameters: the ball-to-powder ratio was set at 10:1, and the rotation speed was fixed at 250 rpm. The milling time was varied up to 80 h, with each composition milled for 1, 4, 10, 30, 60, and 80 hours. 48 XC (0,45 %C, 0,7 %Mn, 0,03 % P, 0,04 %S) steel was used as the substrate. FeSi pre-milled powder with the substrate (ø 25 mm) undergoes milling for 5 hours at a rotation speed of 350 rpm. Subsequently, the material was subjected to a heat treatment at 500°C/800°C for 1 hour. The treatment was conducted in a tubular furnace, specifically the Nabertherm model RHTH 80/300/18 under vacuum conditions. The X-ray diffraction method (Bruker D8 Discover) was used to investigate the phase composition obtained after every milling time. Diffraction tests were recorded with a scanning range (2θ) from 10 to 90° using Cu radiation (λ=1.54 Å) at 40 mA, 40 kV, and 0.02°/step. The evolution of the particle size of the milled powders was investigated by laser diffraction (Mastersizer 2000).

Scanning electron microscopy (SEM) (JEOL- 6780) was employed to understand the in-situ phenomena during MA. The chemical composition of the powders was obtained with X-ray energy-dispersive X-ray spectroscopy (EDS). The thermal behavior was evaluated through differential thermal analysis (DTA). DTA curves were recorded on a Netzsch DTA 404S apparatus using a heating rate of 10°C/min in an argon atmosphere, the examination of coating thickness was determined using optical microscopy (Nikon).

3. Results and Discussion

3.1 Milling of the $Fe_{90}Si_{10}$ and $Fe_{65}Si_{35}$ alloys

Fig. 1 displays the particle size distribution of the $Fe_{90}Si_{10}$ and $Fe_{65}Si_{35}$ mixtures after various milling times, along with powder micrographs.

The $Fe_{90}Si_{10}$ milled powder for 4 and 80 hours (a and b) exhibits a bimodal distribution. In the powder milled 4 hours (Fig. 1 (a)), a prominent peak is marked for the larger particle, accompanied by a smaller peak representing smaller particles. The powder after 80 h (Fig. 1 (b)) exhibits more uniform particle sizes, also the fine particles volume was higher than that after 4 h of milling, and the size of the finest particles obtained after 80 h of milling was 1.81 µm, while the D_{50} reached 6.69 µm. From the SEM micrographs, two populations of varying size can be distinguished for both milled powders (4 and 80 h). The fine particles resulted from the fracture process, and large particle agglomerates formed by cold welding of smaller particles. Extended milling times result in a higher proportion of fine particles, while short milling times result in more agglomerates. The powder after 80 hours of milling shows more uniform particle sizes, suggesting that equilibrium between the welding and fracture processes has been reached. The $Fe_{65}Si_{35}$ mixture (Fig. 1 c and d) displays the same pattern. Particle agglomeration occurred within a short milling time (4 h), resulting in an increase in the mean particle size of 75 µm. Meanwhile, for a long milling time (80 h), a decrease in particle size was observed, with the mean particle size (D_{50}) reaching 6.43 µm. The $Fe_{65}Si_{35}$ powder micrographs demonstrate the impact of milling time on grain size. As shown in Fig. 1 b and d, prolonged milling time promotes refinement of the powder at the expense of agglomeration. Extended milling times lead to a more uniform particle size distribution, while short milling times produce large particle sizes. Comparing both results, the increase in the Si ratio promotes the refinement of the mixture. The agglomerates formed for $Fe_{65}Si_{35}$ were smaller compared to those in the $Fe_{90}Si_{10}$ sample. This result is in good agreement with the results obtained by Bahrami et al.[26] showing the effect of Si on the microstructure during milling. The formation of several populations is related to two processes that occurred during milling: fracturation and agglomeration [27].

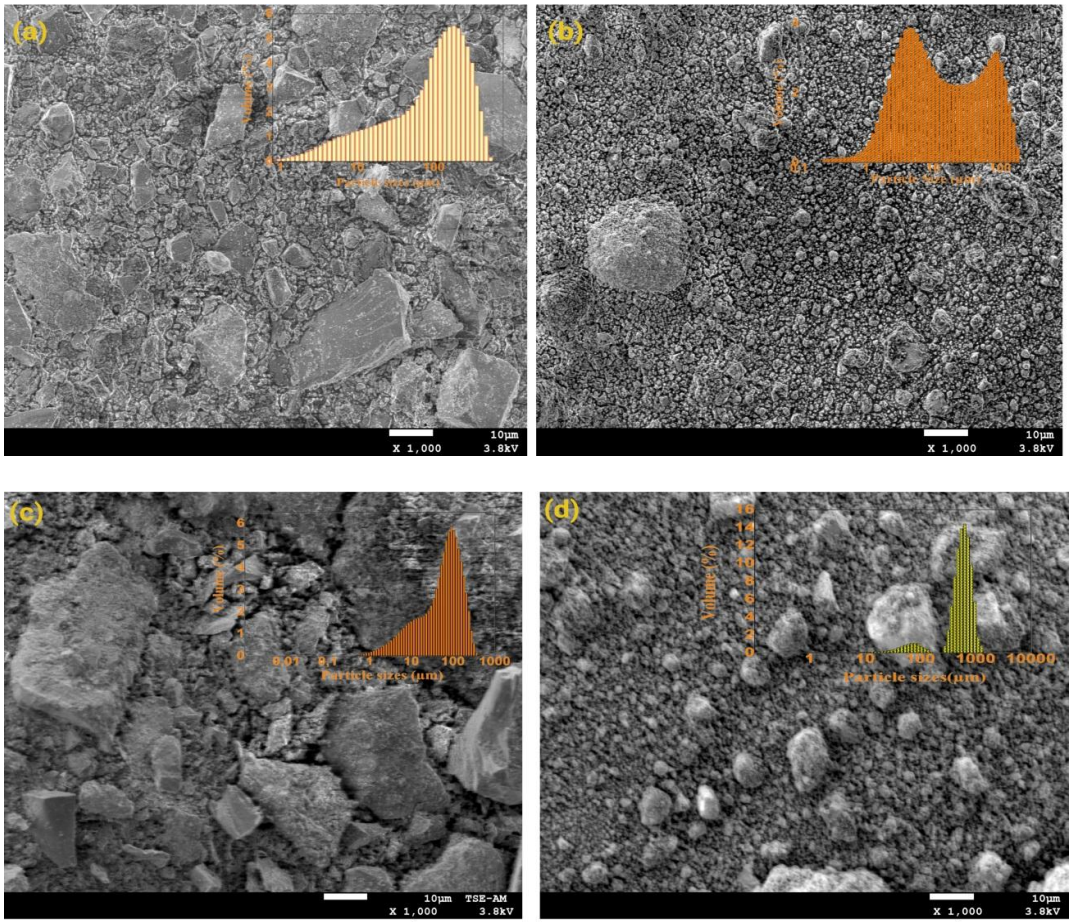

Fig.1. Particle size distribution of milled powder with SEM Micrographs of (a) $Fe_{90}Si_{10}$ milled 4 h, (b) $Fe_{90}Si_{10}$ milled 80 h, (c) $Fe_{65}Si_{35}$ milled 4 h and (d) $Fe_{65}Si_{35}$ milled 80 h.

The latter is more apparent for a short time when the particles of Fe were even ductile. In contrast, the particles become harder for long milling times [28] and tend to dominate the fragmentation process to the detriment of the agglomeration process. The presence of Si increases the brittleness of alloys, which explains the refinement of particles and the diminution of agglomerate volume with $Fe_{65}Si_{35}$. Table 1 summarizes the results of the distribution sizes for both mixture powders. Fig. 2 depicts the X-ray diffraction patterns of the Fe-Si mixture powders as a function of milling time. For $Fe_{90}Si_{10}$ (Fig 2.a), the results revealed the formation of SiO_2 and Fe_2O_3 phases after 1 h, suggesting oxidation of powder. The Fe_xSi_y phases appeared after 10 h of milling, resulting in the formation of Fe_5Si_3 intermetallic and Fe(Si)α solid solution.

Table 1

Particle size distributions for the two mixtures

Composition (wt%)	Milling times (hours)	D_{10} (µm)	D_{50} (µm)	D_{90} (µm)
$Fe_{90}Si_{10}$	1	21,95	122,58	278,33
	4	21,76	109,76	319,94
	10	6,82	74,72	193,65
	30	1,95	8,50	26,99
	60	1,81	6,86	24,06
	80	1,81	6,99	129,61
	1	1,98	9,56	291,80
$Fe_{65}Si_{35}$	4	7,95	75,17	211,96
	10	1,32	15,35	69,90
	30	1,137	12,32	61,76
	60	1,46	11,53	134,86
	80	0,90	6,43	30,36

Additionally, a weak peak corresponding to FeSi was detected. The presence of Fe_3O_4 phase oxide was observed, this is in good agreement with Rifa et al.[29] results, confirming the formation of Fe_2O_3 and Fe_3O_4 during milling. Extending the milling time up to 60 h induces the disappearance of transient phases, as Fe_5Si_3, Fe_2O_3, and SiO_2 substituted by only two principal phases (FeSi and Fe(Si)α). These phases persisted up 80 h of MA. Fig. 2. b shows XRD patterns of $Fe_{65}Si_{35}$ powder milled for different times.

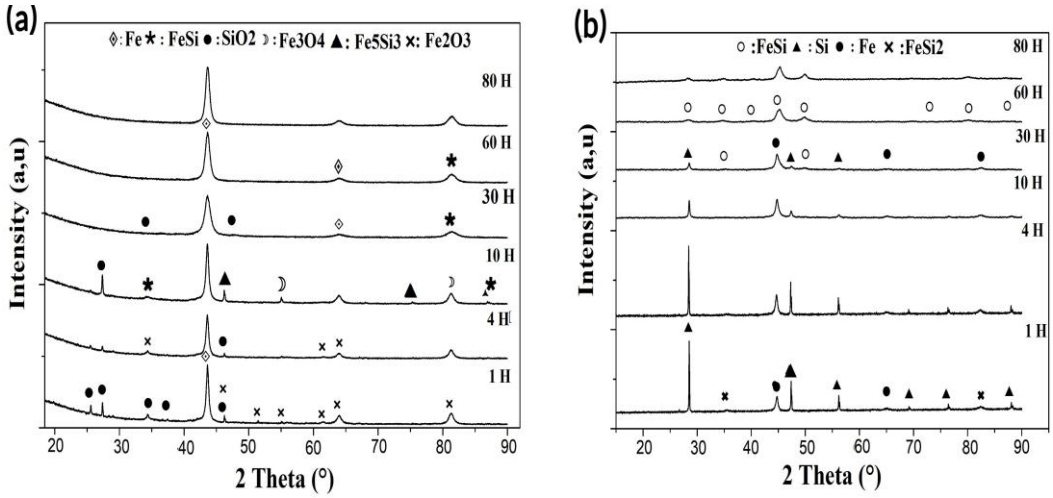

Fig. 2. XRD patterns of the milled powders as function of milling time: (a) $Fe_{90}Si_{10}$: Fe , FeSi, SiO_2, Fe_3O_4 , Fe_5Si_3, Fe_2O_3 phases and (b) $Fe_{65}Si_{35}$: FeSi, Si, Fe, $FeSi_2$ phases.

The results revealed that after 1 h of milling, the $FeSi_2$ phase was formed, and thus, Fe(Si)α solid solution. This result exhibits the ability of Si to increase the reactivity of the Fe-Si mixture. Further prolongation of the milling did not cause any change in the phases formed after 4 and 10 h, while for 30 h of MA, the $FeSi_2$ peaks disappear and are replaced by the FeSi phase peaks. As the process continued up to 60 h, it allowed the achievement of the reaction Fe-Si and, therefore, the formation of only the FeSi phase.

Fig.3. Illustrates the corresponding DTA curves for the $Fe_{90}Si_{10}$ and $Fe_{65}Si_{35}$ mixture powders milled at different times (4 and 80 h).

The DTA curves of $Fe_{90}Si_{10}$ milled for 4 hours (Fig 3.a) showed a broad peak in the temperature range of 400-600°C, caused by internal stresses as interpreted by J.Ding et al. [30]. The endothermic peak at 746°C can be attributed to the ferro-para transition, as confirmed by Abellaoui et al.[20]. Another exothermic peak observed at a temperature of 944°C is related to the transformation of the amorphous phase of the solid solution Fe(Si)α into its crystalline phase [29]. After milling for an extended period (80 hours), the DTA peaks shift towards lower temperatures, which confirm that milling increases the powder's reactivity. As a result, an exothermic peak is observed at 470°C for the $Fe_{90}Si_{10}$ milled powder, corresponding to the amorphous transformation recorded at 944°C with 4 hours of milling. Therefore, the metastable phases revealed by XRD after milling became crystalline.

The DTA (differential thermal analysis) of $Fe_{65}Si_{35}$ (Fig. 3.b) showed an endothermic peak at 750°C that corresponds to the ferro-para transformation. The peak was recorded at a lower temperature (698°C) for the blend that was milled for a longer duration (80 hours) compared to the blend that was milled for a shorter duration (4 hours). This indicates that milling decreases the temperature of the reaction.

The amorphous phase transformation to the crystalline phase was also recorded for this mixture. For the blend milled for 4 hours, the temperature of the reaction was 872°C. However, this peak shifted to a lower temperature with an increase in milling time and eventually attained 449°C.

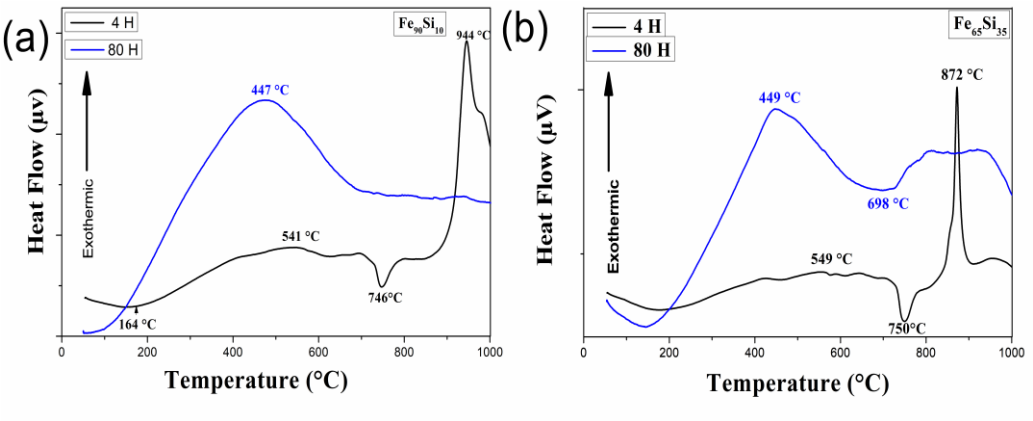

Fig. 3. DTA analysis : a) $Fe_{90}Si_{10}$; b) $Fe_{65}Si_{35}$

3.2- The coating of Fe_xSi_y pre-alloyed on XC steel substrate by co-milling

Macrographs showing the substrate's appearance prior to and during subsequent treatments, as well as the coating process, are shown in Fig. 4. It is evident that the amount of Fe_xSi_y alloyed deposit on XC steel substrates is highly dependent on the length of milling and the post-milling treatment. A larger amount of deposited alloy was indicated by the composite's darker appearance after it was annealed and milled for five hours (fig. 4.f). This implies that the coating process benefits from a longer grinding time. It is also beneficial for the sample that will receive further treatments.

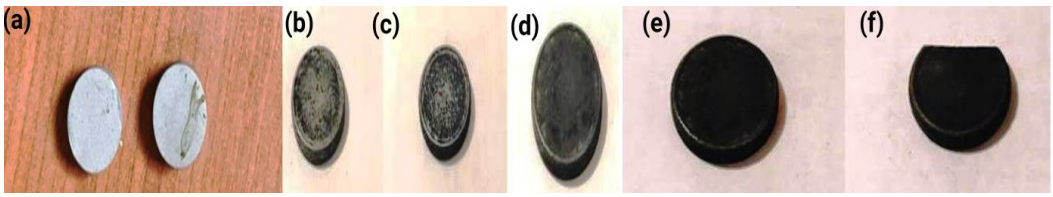

Fig. 4. a)- Substrates XC48 after sand blasting. b)- 1h ; c) 2h ; d) 5 h; e) before annealing; f) after annealing.

Figure 5. illustrates the XRD results for the $Fe_{90}Si_{10}$ coating before and after subsequent treatment, as well as for the $Fe_{65}Si_{35}$ coating after annealing.

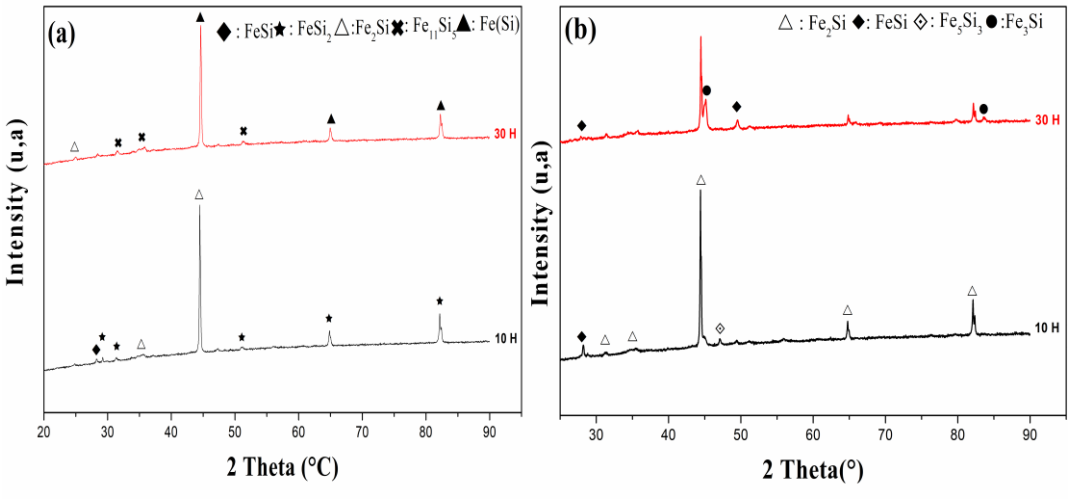

Fig.5 XRD patterns of: a--$Fe_{90}Si_{10}$ coating; b- $Fe_{65}Si_{35}$ coating after annealing at 800°C.

The spectra assigned to $Fe_{90}Si_{10}$ after further treatment showed the development of intermetallics Fe_xSi_y. In the case of the sample milled for 10 hours, we observed the presence of $FeSi_2$, Fe_2Si, and FeSi. For the sample milled for 30 hours, the recorded phases were $Fe_{11}Si_5$, Fe(Si), and Fe_2Si. Figure 9.b confirms the formation of intermetallics in both samples (milled for 10 and 30 hours) with the presence of Fe_2Si and FeSi in both cases, Fe_5Si_3 for 10 hours, and Fe_3Si for 30 hours. By contrasting this with the milled powder's XRD (Fig. 2), we may determine that crystalline coatings have developed. New crystalline intermetallic phases have emerged as a result of the subsequent treatment, which removed the amorphous phases found in the powder following milling:

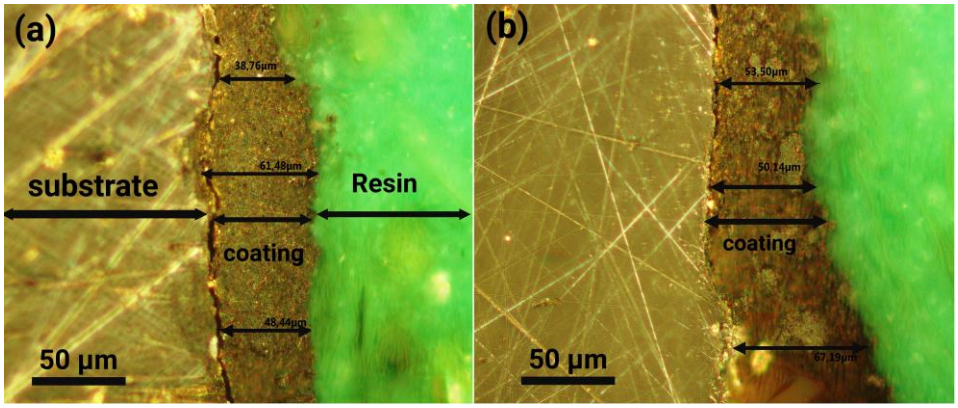

Fig. 6 : Optical images for $Fe_{90}Si_{10}$ coatings : a) 10h milled, b) 30h milled.

The coating morphology of $Fe_{90}Si_{10}$ samples as seen by optical microscopy is shown in Figure 6. Measuring the coating thickness, the $Fe_{90}Si_{10}$

sample milled for 10 hours had an average thickness of 46 µm, whereas the sample milled for 30 hours had an average thickness of 58 µm.

We analyzed the coating-substrate interface using scanning electron microscopy (SEM) to obtain a more thorough understanding of the coating morphologies. The morphology of the coating for $Fe_{90}Si_{10}$ after ten hours of milling is shown in Fig. 7 (a). The element distributions of coating (mapping) are shown in Fig. 7 (b), which validates the existence of high-purity Fe and Si elements. The presence of oxygen points to a possible coating-related oxidation process. Even though it's important to note that the proportion of oxygen found is quite low. The resin that was utilized to prepare the SEM analysis is what is responsible for the carbon's presence. Three sub-layers are discernible: the first is made up of tiny Fe_xSi_y particles that are bonded to the substrate, the second is made up of aggregated silicon oxide grains, and the third is made up of bigger Fe_xSi_y grains that are larger than those in the first sub-layer. Fine-grained FeSi makes up the first layer, which promoted fast diffusion and the subsequent two layers' development. Compared to FeSi, silicon is a metalloid with a less complicated structure, which gives silicon atoms more mobility and accelerates diffusion. This metalloid makes up the second layer. It's important to note that after annealing, the silicon reacted with oxygen atoms to form a SiO_2 sub-layer.

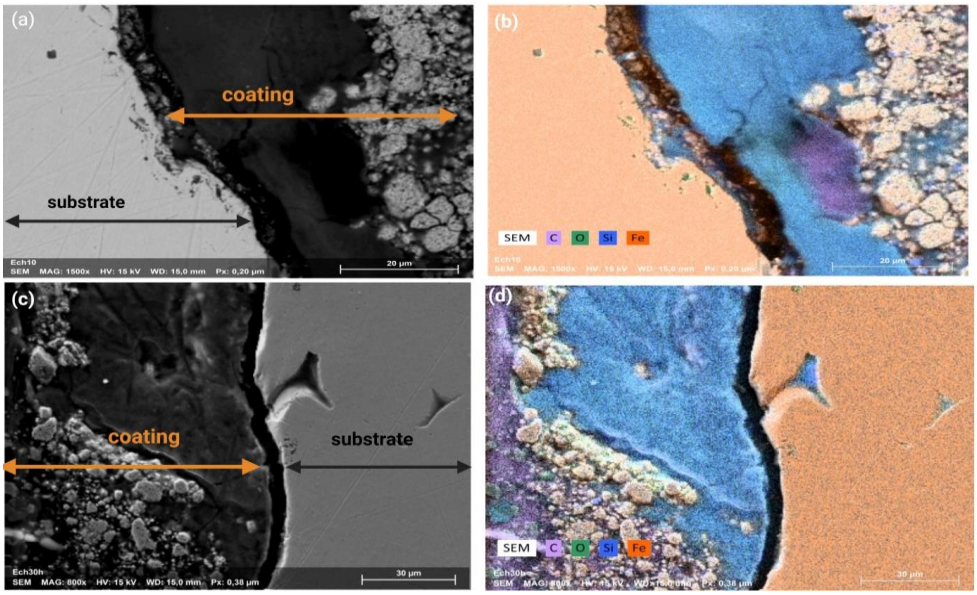

Fig. 7. Scanning electron microscopy analysis for $Fe_{90}Si_{10}$ milled 10h : a) :cross-section substrate-coating, b) : Mapping ; For $Fe_{65}Si_{35}$: c): cross-section substrate-coating, d) :mapping.

The coating behavior was assessed using hardness tests, and the results are presented in Table 2. The table includes the hardness values for each coating, as well as the hardness of the bare substrate after annealing, which serves as a

control. 48 XC steel exhibits a hardness of 280 HV. Annealing has a softening effect on materials, as seen in the substrate without coating, which recorded an average hardness of 212 HV. This decrease in hardness is typical of annealing, where the material tends to soften due to grain growth. However, all three coatings demonstrated an enhancement in hardness, with values higher than the baseline 212 HV. This improvement is indicative of the quality of the coatings. Furthermore, the Hall-Petch effect is observed in Table 2, where finer grain sizes, associated with $Fe_{65}Si_{35}$ powders milled for 30 hours (table 1), correspond to higher hardness values. The extended milling time resulted in narrower D10 and D50 distributions, leading to finer grain sizes and consequently improved hardness. In contrast, powders milled for only 10 hours exhibited broader particle size distributions (D10 and D90 values) (table 1), resulting in larger grains and lower hardness. This explains the observed variation in hardness. The relationship between hardness and grain size follows Hall-Petch, with hardness increasing as grains get smaller [48].

Table 2.

Hardness values of Fe_xSi_y coating after annealing Samples

Samples	The hardness of the substrate in its uncoated state (48 XC) After annealing (HV)	Hardness of Coatings after annealing (HV)
$Fe_{90}Si_{10}$ 10 h	212,5	255.5
$Fe_{90}Si_{10}$ 30h		274.5
$Fe_{65}Si_{35}$ 10h		332
$Fe_{65}Si_{35}$ 30h		466.5

6. Conclusions

In this study, we developed FeSi nanostructured alloy coatings using high-energy ball milling on 48 XC steel. Several factors were found to impact the formation of these intermetallic coatings. Prolonged milling times led to increased solubility of Si in the Fe system, resulting in the formation of homogeneous phases of intermetallic FeSi and Fe(Si)α solid solution. Furthermore, adding larger Si percentages (such as 35% Si) raised the mixture's reactivity and caused new intermetallic phases to form during a short milling time. The FeSi phase eventually developed as a result of prolonged grinding. It's important to note that combinations containing more Si exhibited brittle behavior compared to mixtures containing less Si, which resulted in the milling process producing finer powder. One of the most significant findings of this study is that it demonstrates the feasibility of creating coatings from alloyed powders Fe_xSi_y on 48 XC steel

through high-energy ball milling. Across all samples, the coatings showed improved mechanical properties, particularly in terms of hardness, where values increased even after annealing. The sample that was ground for 30 hours showed that the high hardness that was detected was greatly influenced by the presence of tiny particles.

R E F E R E N C E S

1. *C. Suryanarayana,* Mechanical alloying: a critical review, Mater. Res. Lett., **vol. 10**, no. 10, May. 2022, pp. 619-47.
2. *M. Javdan, K. Gheisari, M. Reihanian*, Mechanically alloyed (FeCoNi) 75Cu25− xSix high entropy alloys: phase evaluation and magnetic properties, J. Alloys Compd., **vol 952,** August. 2023, p. 170030.
3. *C. Shuai, C. He, G. Qian, A. Min, Y. Deng, W. Yan*g, et X. Zang, Mechanically driving supersaturated Fe–Mg solid solution for bone implant: preparation, solubility and degradation, Compos B: Eng., **vol. 207**, February. 2021, p. 108564.
4. *C. Shuai, C. He, S. Peng, F. Qi, G. Wang, A. Min, W. Yang, and W.Wang*, Mechanical alloying of immiscible metallic systems: process, microstructure, and mechanism, Adv. Eng. Mater., **vol. 23**, no. 4. February. 2021, p. 2001098.
5. B. *Avar, T.Simsek, S.Ozcan, A.K. Chattopadhyay, B.Kalkan*, Structural stability of mechanically alloyed amorphous $(FeCoNi)_{70}Ti_{10}B_{20}$ under high-temperature and high-pressure, J. Alloys Compd., **vol. 860**, April. 2021, p. 158528.
6. *R. John, A. Karati, J. Joseph, D. Fabijanic, B.S Murty*, Microstructure and mechanical properties of a high entropy alloy with a eutectic composition ($AlCoCrFeNi_{2.1}$) synthesized by mechanical alloying and spark plasma sintering, J. Alloys Compd., **vol .835**, September. 2020, p. 155424.
7. *Y. Liu, D. Chabane, O. Elkedim,* Intermetallic compounds synthesized by mechanical alloying for solid-state hydrogen storage: a review, Energies. **vol. 14,** no. 18, September 2021, p.5758.
8. *E.B. Moustafa, M.A. Taha*, Preparation of high strength graphene reinforced Cu-based nanocomposites via mechanical alloying method: Microstructural, mechanical and electrical properties, Appl. Phys. A., **vol. 126**, no. 3, February 2020, p. 220.
9. *A. Obeydavi, A. Shafyei, A. Rezaeian, P. Kameli, J.W. Lee*, Microstructure, mechanical properties and corrosion performance of $Fe_{44}Cr_{15}Mo_{14}Co_7C_{10}B_5Si_5$ thin film metallic glass deposited by DC magnetron sputtering, J.Non-Cryst. Solids., **vol. 527**, January. 2020, p. 119718.
10. *K.G. Prashanth*, Crystallization and growth kinetics of $Zr_{65}Cu_{25}Ni_5Ag_{2.5}Al_{2.5}$ glass", Mater. Des. Process. Commun., **vol. 2**, no 3, January. 2020, p. e137.
11. *A. Mameri, S. Azem, A. Bilek*, Synthesis of metallic and intermetallic matrix composites reinforced by alumina by reaction in NiO/Al mixtures, Trans. Indian Inst. Met., **vol 71,** September 2018, pp.727-36.
12. *A. Mameri, I. Daoud, A. Rezzoug, S. Azem, R. Yamanoglu*. Tribological properties of in situ oxide reinforced nickel matrix composites produced by pressure-assisted sintering. J. Adv. Manuf. Technol., **vol 120**, no 5, March. 2022; pp. 3731-40.
13. *S. Lee, J. Kim, C. J. Lee*, Reactivity enhancement and fabrication of Al-MoO_3 thermite coating using ball milling for kinetic spraying", J. Therm. Spray Technol., **vol 29**, July. 2020 ; no 7, pp. 1669-1681.
14. *P. Novák, D. Benediktová, S. Mestek, A. Tsepeleva, J. Kopeček,* Compounds. Aluminum alloys with natural ratio of alloying elements manufactured by powder metallurgy, J. Alloys Compd., **vol 931**, January 2023, pp. 167440.
15. *B. Zuo, N. Saraswati, T. Sritharan, H.H. Hng*, Production and annealing of nanocrystalline Fe–Si and Fe–Si–Al alloy powders. Mater. Sci. Eng: A., **vol 371**, no (1-2), April. 2004; pp. 210-216.
16. *B. Shen, Y. He, Z. Wang, L. Yu, Y. Jiang, H. Gao*, Reactive synthesis of porous FeSi intermetallic compound, J. Alloys Compd, **vol 826,** June 2020; p154227.

17. *E. Gaffet, N. Malhouroux, M. Abdellaoui*, Far from equilibrium phase transition induced by solid-state reaction in the Fe-Si system, J. Alloys. Compd., **vol 194**, no 2, May 1993, pp. 339-360.
18. *A.G. Escorial, P. Adeva, M. Cristina, A. Martin, F. Carmona, F. Cebollada, , V.E Martín , M Leonato, J.M González*, Ball milling mechanical alloying in the Fe100− xSix system. Mater. Sci. Eng: A., **vol 134**, March 1991, pp: 1394-1397.
19. *N. Ševulová, A. Buchal, P. Petrovič, K. Tkáčová, V. Šepelák*, Structural investigation of the high-energy milled Fe–Si system. J. Magn. Magn. Mater ., **vol 203**, no (1-3), August 1999; pp.190-200.
20. *M. Abdellaoui, T. Barradi, E. Gaffet*, Mechanism of mechanical alloying phase formation and related magnetic and mechanical properties in the Fe-Si system, J. Alloys.Compd., **vol 198**, no (1-2), August 1993, pp.155-164.
21. *S.H. Kim, Y.J. Lee, B.H Lee, K.H. Lee, K. Narasimhan, Y. Do Kim*, Characteristics of nanostructured Fe–33 at.% Si alloy powders produced by high-energy ball milling, J. Alloys Compd., **vol 424** , no(1-2), November. 2006, pp. 204-208.
22. *T. Zhou, J. Zhang, J. Xu, Z. Yu, G. Gu, D. Wang, H. Huang, Y. Du, J. Wang, Y.Jiang*, Preparation of nanocrystalline Fe-Si alloys and their magnetic properties. Journal of Magnetism and Magnetic Mater., **vol 164**, no (1-2), November 1996; pp. 219-224.
23. *C. Stanciu, J.M. da Cunha, I. Chicinaş,* O. *Isnard*, Structural, magnetic and Mössbauer spectroscopy characterisation of the Fe-15 wt% Si nanocrystalline powder obtained by mechanical alloying and annealing, J. Alloys Compd., **vol** 797, August .2019,pp. 865-873.
24. *G. Gupta, K. Mondal, R. Balasubramaniam*, In situ nanocrystalline Fe–Si coating by mechanical alloying, J. Alloys.Compd., **vol 482**, no (1-2), August 2009, pp.118-122.
25. *Y. Li, C. Chen, R. Deng, X. Feng, Y. Shen*, Microstructure evolution of Cr coatings on Cu substrates prepared by mechanical alloying method, Powd. Tech., **vol 268,** December 2014, , pp. 165-172.
26. *A. Bahrami, S. Sharafi, H. Baghbaderani*. The effect of Si addition on the microstructure and magnetic properties of Permalloy prepared by mechanical alloying method, Adv. Powd. Techn., **vol** 24, **no (1),** January 2013; pp 235-241.
27. *P. Novák, T. Kubatík, J. Vystrčil, R. Hendrych, J. Kříž, J. Mlynár, D.Vojtěch*, Powder metallurgy preparation of Al–Cu–Fe quasicrystals using mechanical alloying and spark plasma sintering, Intermetallics., **vol 52**,September 2014; pp. 131-7.
28. *N. Khitouni, R. Daly, J.J. Suñol, L. Escoda, M. Khitouni* , Effect of Silicon Additions on Structural and Microstructural Properties of Nanostructured FeCoNi Alloy Prepared by High-Energy Ball Milling , Silicon., **vol 15**, no 4, October 2023; pp 1977-1986.
29. *M. Rifai, Y. Yunasfi, E. Sukirman, Y. Sarwanto, M. Mujamilah*, Structure and Magnetic Properties Of Fe/Si Nanoparticles Prepared by High Energy Milling Process, Indones. J. Appl. Phys., **vol 11**, no 2, October 2021, pp 239-247.
30. *J. Ding, Y. Li, L. Chen, C. Deng, Y. Shi, Chow Y, T.B. Gang*, Microstructure and soft magnetic properties of nanocrystalline Fe–Si powders, J. Alloys Compd., **vol 314**, no (1-2), January 2001, pp 262-267.
31. *O. Kubaschewski*. Iron—Binary phase diagrams: Springer Science & Business Media; March 2013.